Support Information

Ultrathin MoS_2-Decorated N-Doped Carbon with Hierarchical Porosity for High-Capacity, Low-Energy Capacitive Deionization with Outstanding Cycling Stability

Mai A. Hassan[† a, b, c], Manar M. Taha[† d], Gehad Hamdy [b, c], F. A. Taher [b, c], Nageh K. Allam [a, *]

[a] Energy Materials Laboratory (EML), Physics Department, School of Sciences and Engineering, The American University in Cairo, New Cairo 11835, Egypt

[b] Chemistry Department, Faculty of Science, Al-Azhar University (Girls), Cairo, Egypt

[c] Al-Azhar Technology Incubator (ATI), Al-Azhar University (Girls), Cairo, Egypt

[d] Environmental Research Department, Soils, Water, and Environment Research Institute, Agricultural Research Center, Giza, Egypt

*Corresponding Author's Email: nageh.allam@aucegypt.edu

† Equal contribution.

Contents:

Materials Characterization

The morphology and microstructure of the electrodes were examined using a field-emission scanning electron microscope (FESEM, Zeiss Ultra 60) operated at 5 kV and equipped with an Oxford ISIS 310 energy-dispersive X-ray (EDX) detector for elemental analysis. High-resolution transmission electron microscopy (HR-TEM, JEM-2100 Plus, JEOL, Tokyo, Japan) operating at 200 kV was employed to investigate nanoparticle morphology and lattice features. TEM measurements were conducted at the Faculty of Science, Al-Azhar University. Crystalline phases were identified using X-ray diffraction (XRD, PANalytical Empyrean) with Cu Kα radiation (λ = 0.15418 nm, 40 kV, 30 mA). Raman spectra were recorded using a Pro Raman-L Analyzer dispersive Raman microscope (λ_{exc} = 512 nm, 1 mW). Surface elemental composition and chemical states were analyzed by X-ray photoelectron spectroscopy (XPS, Thermo Scientific ESCALAB 250Xi) using Al Kα radiation. Nitrogen adsorption–desorption isotherms were measured at 77 K using a Quanta Chrome Nova 3200e analyzer. Prior to analysis, samples were degassed overnight at 393 K under vacuum. Fourier-transform infrared (FTIR) spectra were collected using a Vertex 70 spectrometer equipped with an attenuated total reflection (ATR) accessory. The specific surface area (SSA) was calculated by the Brunauer–Emmett–Teller (BET) method, while pore size distribution was determined using the Barrett–Joyner–Halenda (BJH) model.

Electrochemical testing

The electrochemical properties of MoS_2, NDC, and MoS_2/NDC electrodes were evaluated by cyclic voltammetry (CV), galvanostatic charge–discharge (GCD), and electrochemical impedance spectroscopy (EIS) using a Biologic SP-300 potentiostat. Measurements were conducted in a three-electrode configuration with 1 M NaCl aqueous electrolyte, pre-purged with inert gas to minimize

dissolved oxygen interference. The working electrodes were prepared by mixing the active material, acetylene black (AB), and PVDF binder in a mass ratio of 8:1:1. The slurry was drop-cast onto a graphite sheet (1 × 1 cm² active area) and dried at 60 °C for 12 h. Graphite substrates were cleaned with ethanol prior to coating. The mass loading was maintained at 0.8–1.0 mg cm^{-2}. A graphite rod and a saturated calomel electrode (SCE, saturated KCl) served as the counter and reference electrodes, respectively. The specific capacitance was calculated from CV and GCD data using:

$$C_{CV} = \frac{\int I\, dV}{v\, m\, \Delta V} \qquad \textbf{(Eq.}S1\textbf{)}$$

$$C_{GCD} = \frac{I\, \Delta t}{m\, \Delta V} \qquad \textbf{(Eq.}S2\textbf{)}$$

where *m* is the active mass (g), *I* is the current (A), *v* is the scan rate (V s^{-1}), and ΔV is the potential window (V). The EIS-derived capacitance (C_i) was obtained from:

$$C_i = \left|\frac{1}{\omega Z''}\right| \qquad \textbf{(Eq.}\ S3\textbf{)}$$

where ω is the angular frequency and Z" is the imaginary impedance component.

The potential of zero charge (E_{PZC}) was determined from EIS measurements conducted at different applied potentials in deaerated 5 mM NaCl electrolyte over a frequency range of 0.1–100 Hz with a 5 mV sinusoidal perturbation [27].

*in order to distinguish the electric-double layer contribution in the total capacitance, the Trassaiti method was applied (**Eq. S4** and **S5)*** 7,8.

$$q = const. * \sqrt{v}^{-1} + C_{dl} \qquad \textbf{(Eq. S4)}$$

$$q^{-1} = Const. * \sqrt{v} + \frac{1}{C_T} \qquad \textbf{(Eq. S5)}$$

where q is the charges in Columbus, $\sqrt{v}$ is the square root of scan rate, C_{dl} is the double-layer capacitance, C_T is the total capacitance.

Single-Pass CDI Testing

Desalination performance was assessed using a bench-scale single-pass, flow-by CDI cell. This configuration was selected to suppress local pH gradients near the negatively polarized electrode and enhance operational stability [28,29]. Electrodes were fabricated by mixing active material, PVDF, and carbon black in a weight ratio of 80:10:10. The mixture was homogenized using an agate mortar and dispersed in DMF under continuous stirring overnight. The slurry was coated onto a 7 × 6 cm² graphite sheet using a K303 RK Printcoat multi-coater (120 μm rod). The coated electrodes were air-dried and further dried at 60 °C for 12 h. Graphite sheets were pre-cleaned with ethanol. The electrode mass loading was approximately 500 mg.

The CDI cell consisted of two identical electrodes assembled symmetrically within an acrylic housing. Saline feed solution (700 μS cm^{-1} NaCl) was circulated from a 50 L reservoir using a Cole-Parmer Masterflex peristaltic pump. Effluent conductivity was continuously monitored using HI1131 probes connected to a HANNA HI5522-01 multi-meter, with data recorded every 30 s.

Adsorption/desorption cycles were performed with charging/discharging durations of 80 min. Regeneration was conducted at zero applied voltage using feed solution (700 μS cm^{-1}) at 40 mL min^{-1}. Prior to measurements, electrodes were conditioned by three preliminary cycles [27]. CDI performance was evaluated at applied voltages of 0.8–1.6 V and flow rates of 20–60 mL min^{-1}. Long-term cycling stability was assessed at 1.4 V for 350 cycles. The salt adsorption capacity (SAC), average salt adsorption rate (ASAR, η), and charge efficiency (Λ) were calculated using:

$$SAC = \frac{\int C(t)\,\Phi\,dt}{m} \qquad \textbf{(Eq. S6)} \qquad \eta = \frac{\Gamma}{t}$$

$$\Lambda = \frac{\Gamma F}{\Sigma \int I dt} \times 100 \qquad \textbf{(Eq. S7)} \qquad \textbf{(Eq. S8)}$$

$$\text{Energy consumption} = V * \int_0^{te} \int idt_e / m_e \qquad \textbf{(Eq.S9)}$$

where C is the concentration (mg L^{-1}), Φ is the flow rate (L s^{-1}), m is the total active mass (g), Γ is the adsorbed salt (mol g^{-1}), and F is Faraday's constant (96,486 C mol^{-1}), V applied voltage, i current, t_e time at equilibrium m mass of two electrodes in kg.

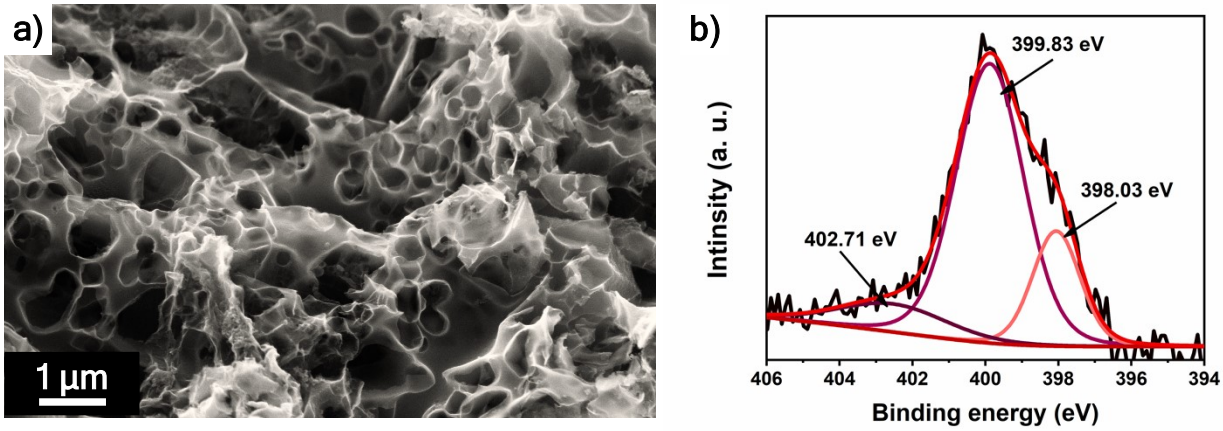

Figure S1. a) SEM and b) XPS of N1s of nitrogen doped carbon (NDC) pyrolysis at 750 °C.

The N 1s XPS peaks of NDC at 398.03, 399.8, and 402.7 eV shift to 398.7, 400.5, and 403.6 eV in NDC@MoS_2. These upward shifts indicate electron density transfer from NDC to MoS_2, confirming strong interlayer interaction. This interaction alters the local electronic environment of nitrogen atoms, increasing the availability of electrons for cation adsorption. As a result, the composite exhibits enhanced charge efficiency and higher salt adsorption in CDI applications, demonstrating that the electronic configuration tuning directly improves desalination performance.

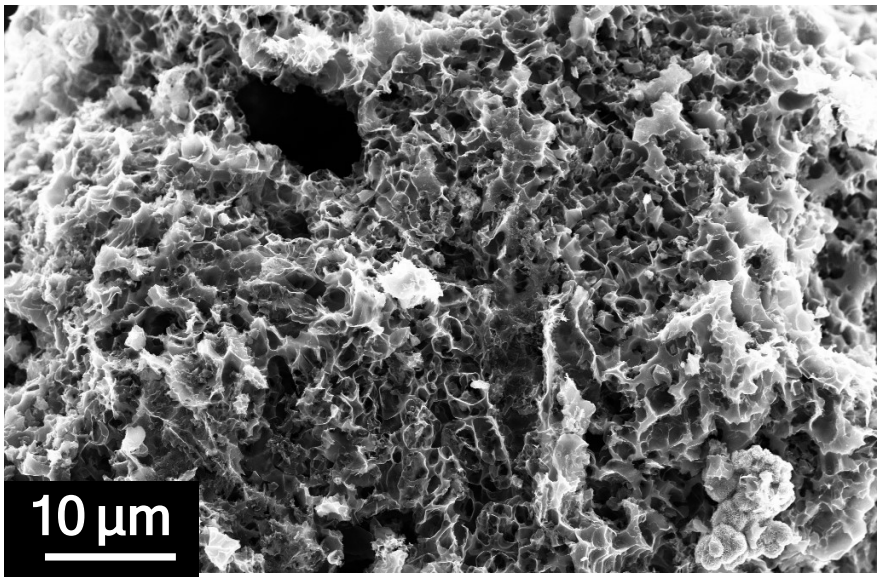

Figure S2. SEM at low magnification of MoS_2-NDC

Table S1:

Material	**Peak Assignment**	**Binding Energy (eV)**	**FWHM (eV)**	**Area (CPS·eV)**	**Atomic %**
Pristine MoS_2	Mo $3d_{5/2}$	228.78	1.47	4652.05	30.1
	Mo $3d_{3/2}$	232.31	2.7	9028.34	58.51
	Mo^{6+} (defect)	235.93	1.53	1754.5	11.39
MoS_2/NDC	Mo $3d_{5/2}$	232.7	1.65	314.95	67.17
	Mo $3d_{3/2}$	235.75	1.59	153.71	32.83

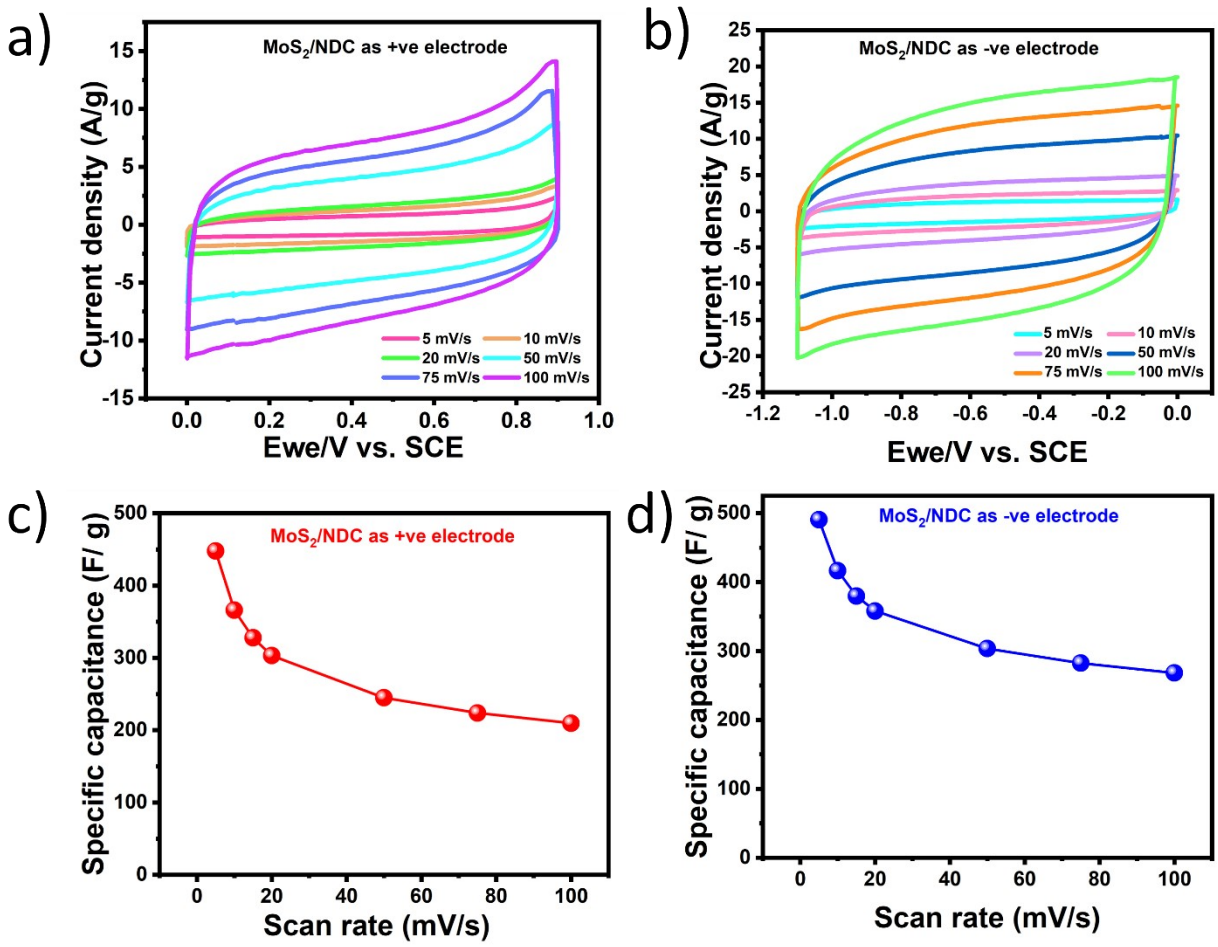

Figure S3. (a) CV and (b) corresponding specific capacitance of the *MoS_2–NDC* as a potential negative and positive electrode, respectively.

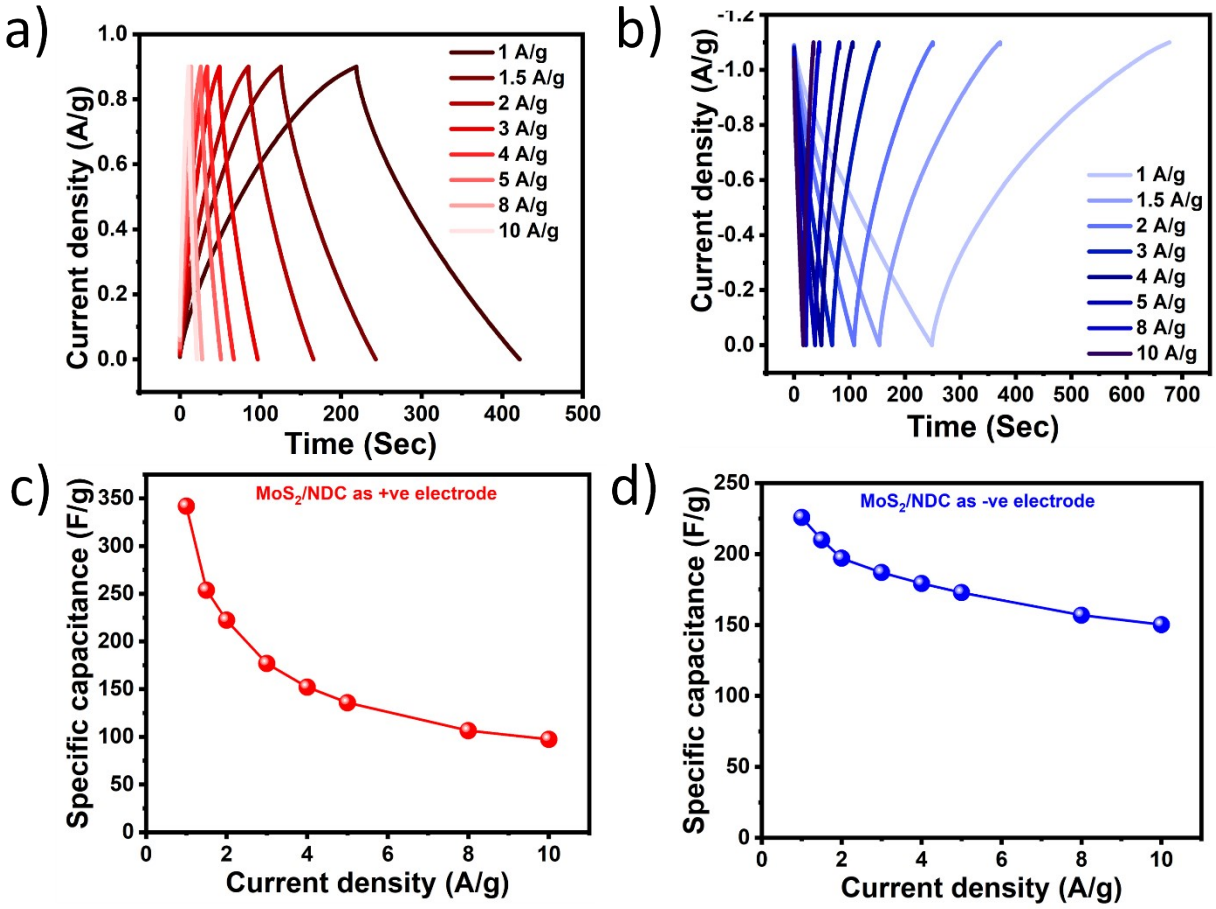

Figure S4. (a) GCD and (b) corresponding specific capacitance of the *MoS_2–NDC* as a potential negative and positive electrode, respectively.

Table S2

Electrode	Rs (Ω)	Rct (Ω)
MoS_2	5.10	1.34
NDC	6.5	1.1
MoS_2–NDC	6.28	0.80

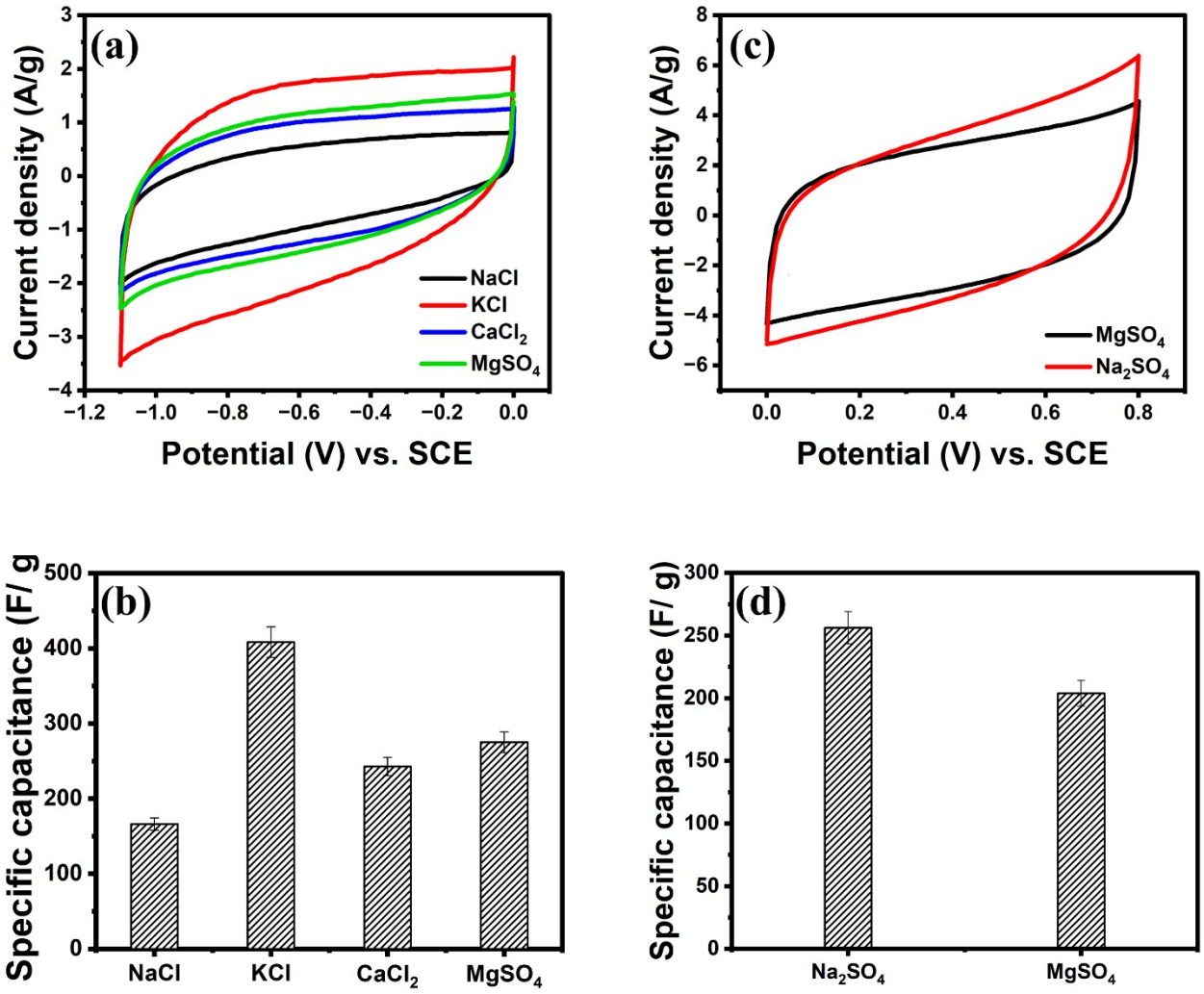

Figure S5. Electrochemical performance of the electrode in different electrolytes with 0.5 M concentration (a) Cyclic voltammetry curves recorded in NaCl, KCl, $CaCl_2$, and $MgSO_4$ electrolytes within the negative potential window, showing distinct current responses depending on ion type. (b) Corresponding specific capacitance values, indicating superior performance in KCl electrolyte. (c) Cyclic voltammetry curves measured in Na_2SO_4 and $MgSO_4$ within the positive potential window, highlighting higher current response in Na_2SO_4. (d) Calculated specific capacitance values, confirming enhanced capacitive behavior in Na_2SO_4 compared to $MgSO_4$.

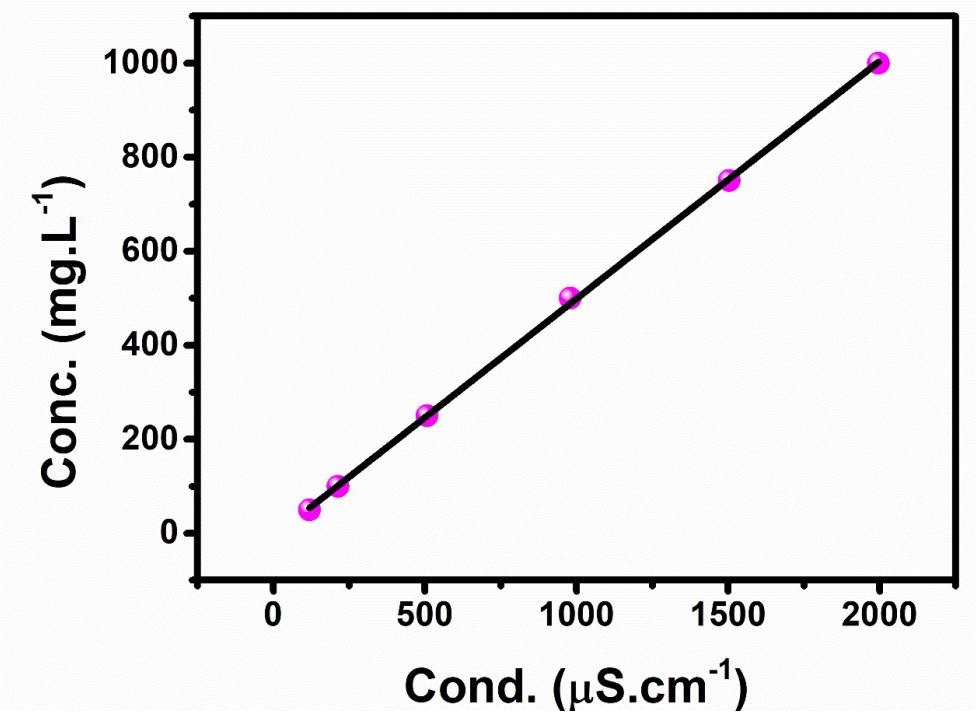

Figure S6. The Calibration of the Conductivity to NaCl Concentration.

The calibrated Equation 1 of Conductivity-Concentration is:

$$Conc, mg.L^{-1} = 0.5056 \times Cond, \mu S.cm^{-1} - 6.5988$$

where the R^2=0.9998 indicates that the solution's salinity can be considered a linear dependent to the conductivity.

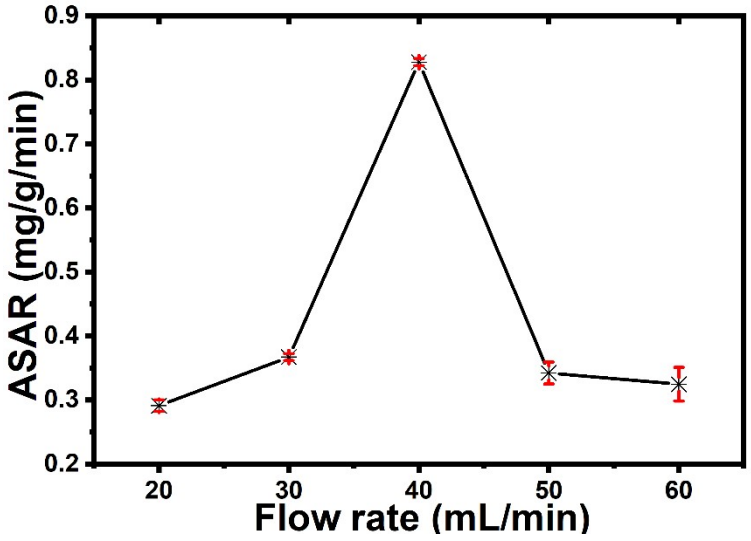

Figure S7. The Conductivity profiles (μS/cm) of flow rate of the symmetric CDI cell.

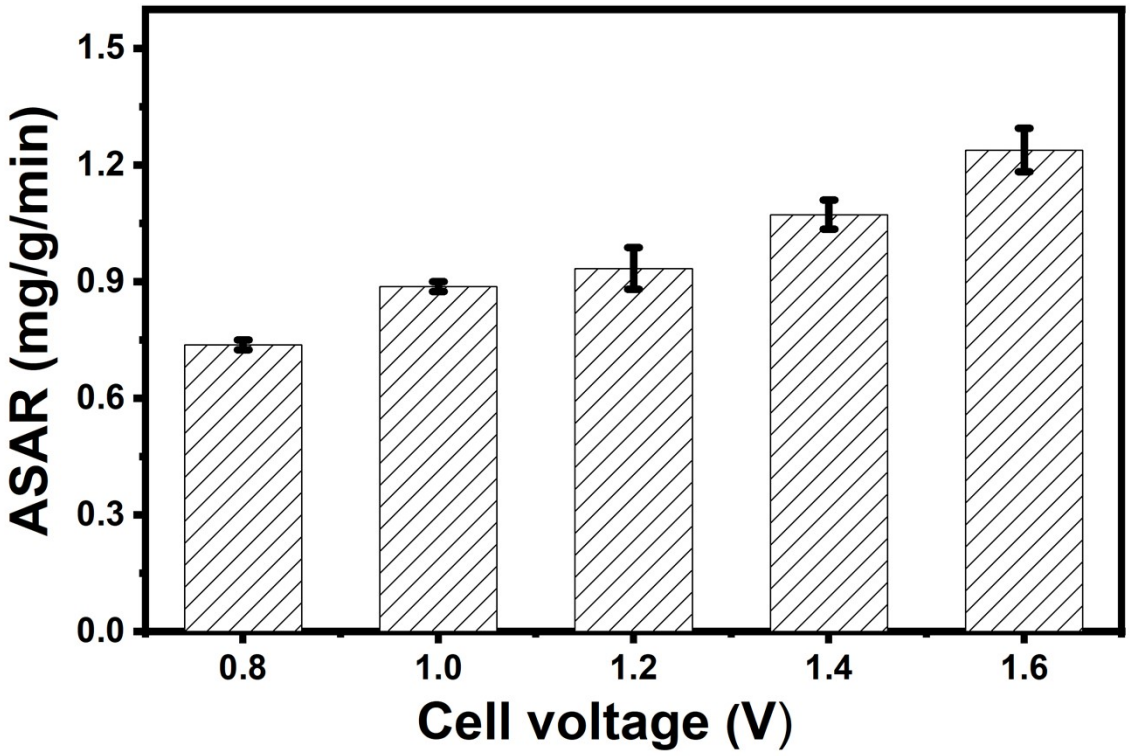

Figure S8. Average salt adsorption capacity at diff voltages.

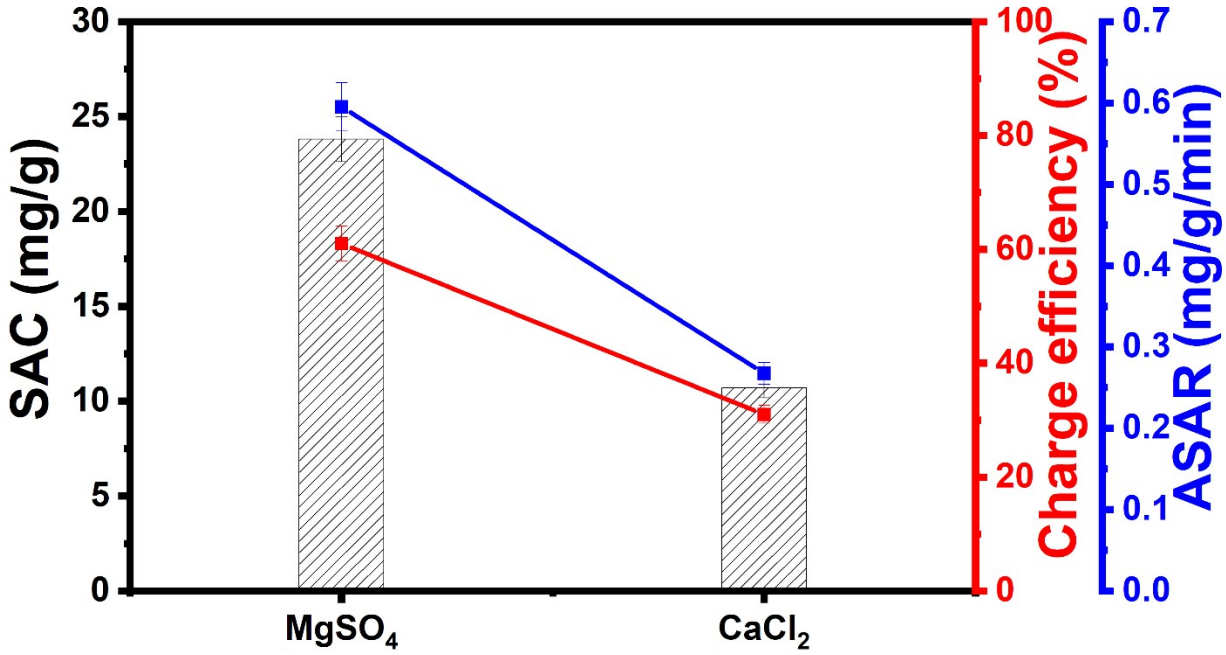

Figure S9. Capacitive deionization performance of the electrode in terms of salt adsorption capacity (SAC), charge efficiency (Λ), and average salt adsorption rate (ASAR) of $MgSO_4$ and Ca_2Cl

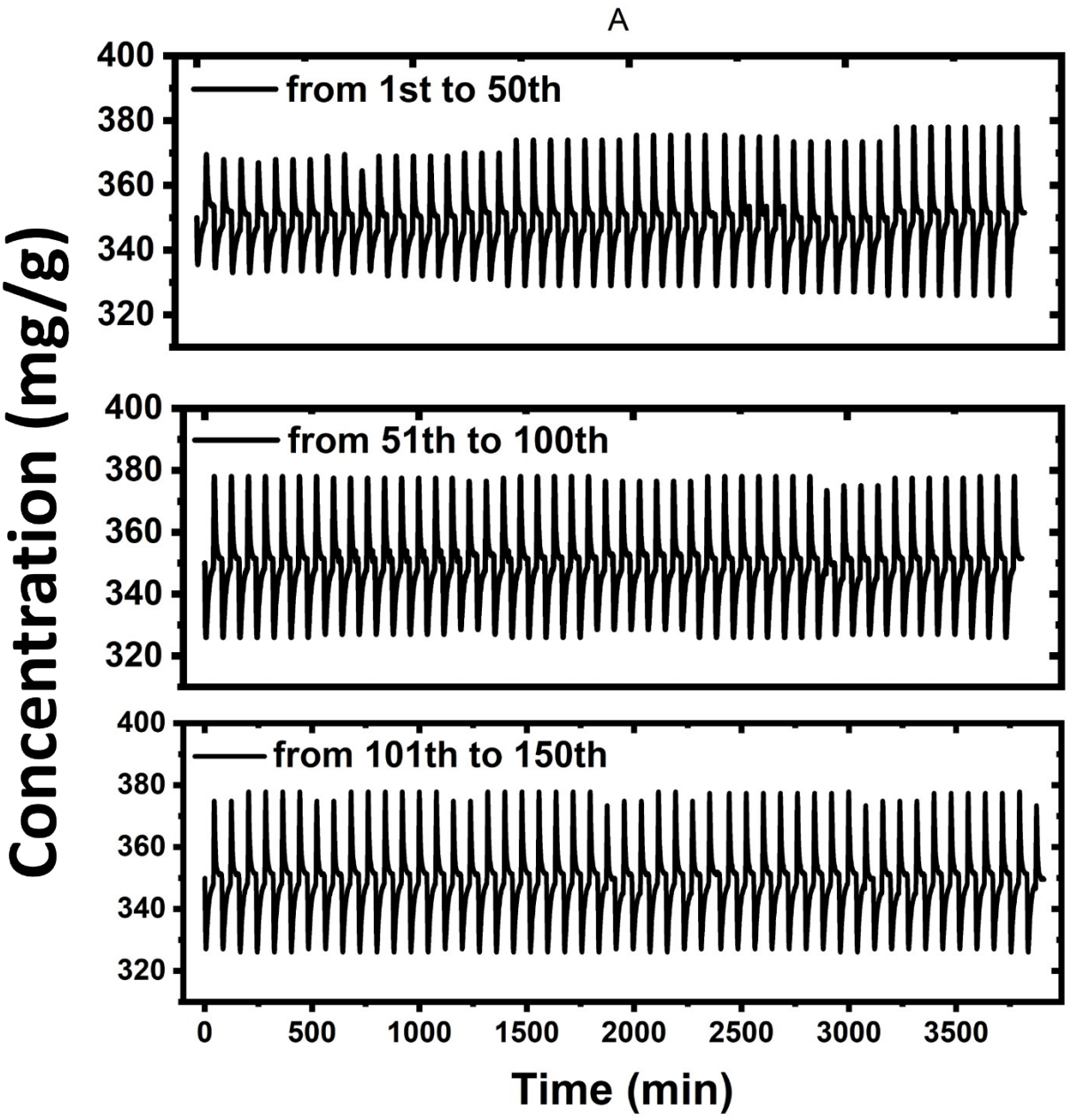

Figure S10. Charge–discharge concentrations profiles of the MoS_2–NDC composite electrodes recorded over stability cycles 1-150.

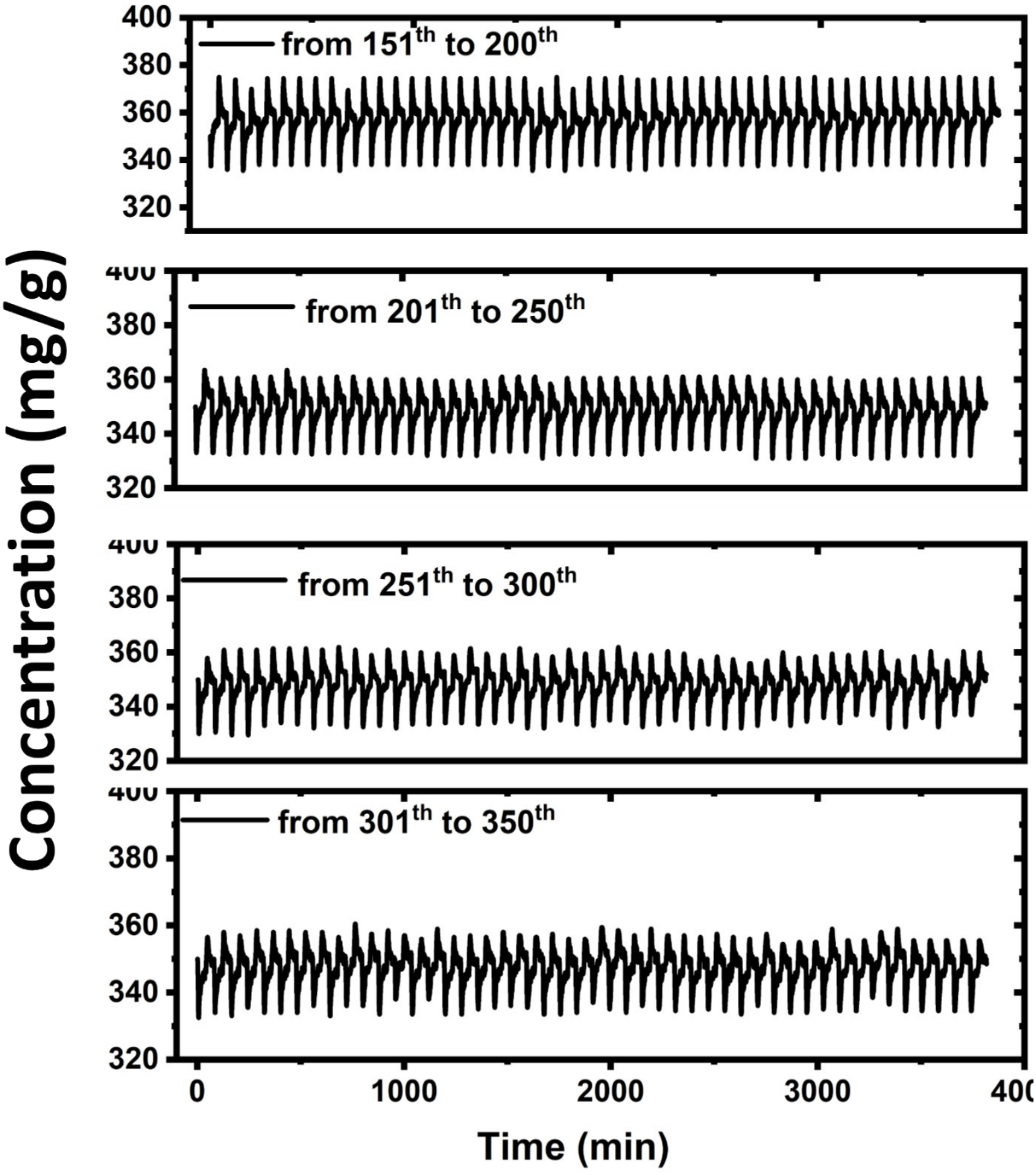

Figure S11. Charge–discharge concentrations profiles of the MoS_2–NDC composite electrodes recorded over stability cycles 151–350.

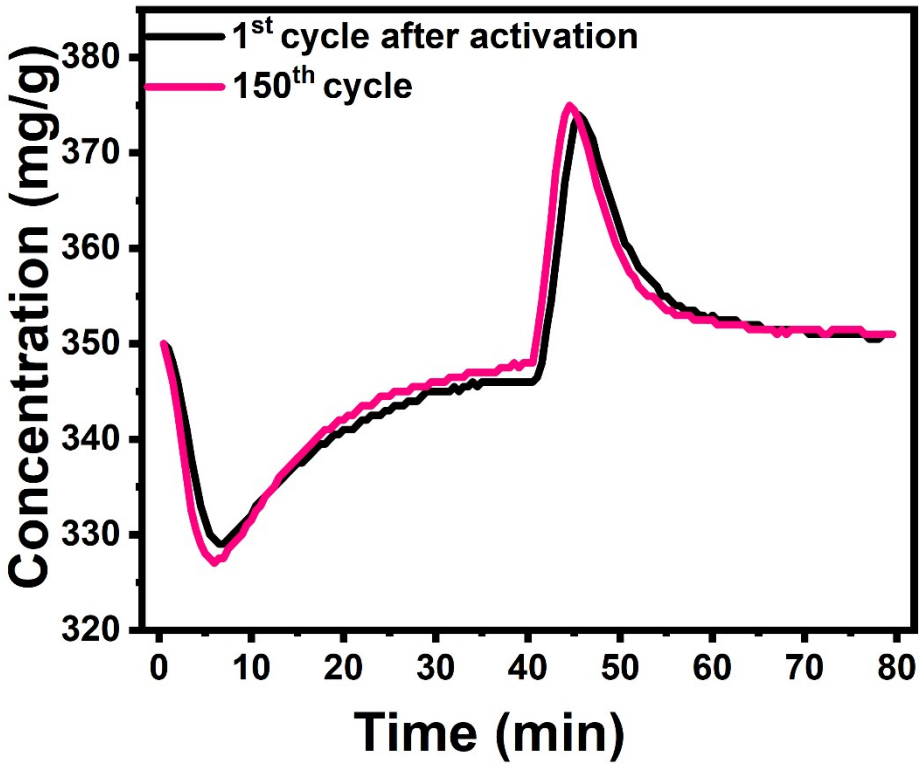

Figure S12. Conductivity profile of the full cycle of first cycle after activation and last cycle.

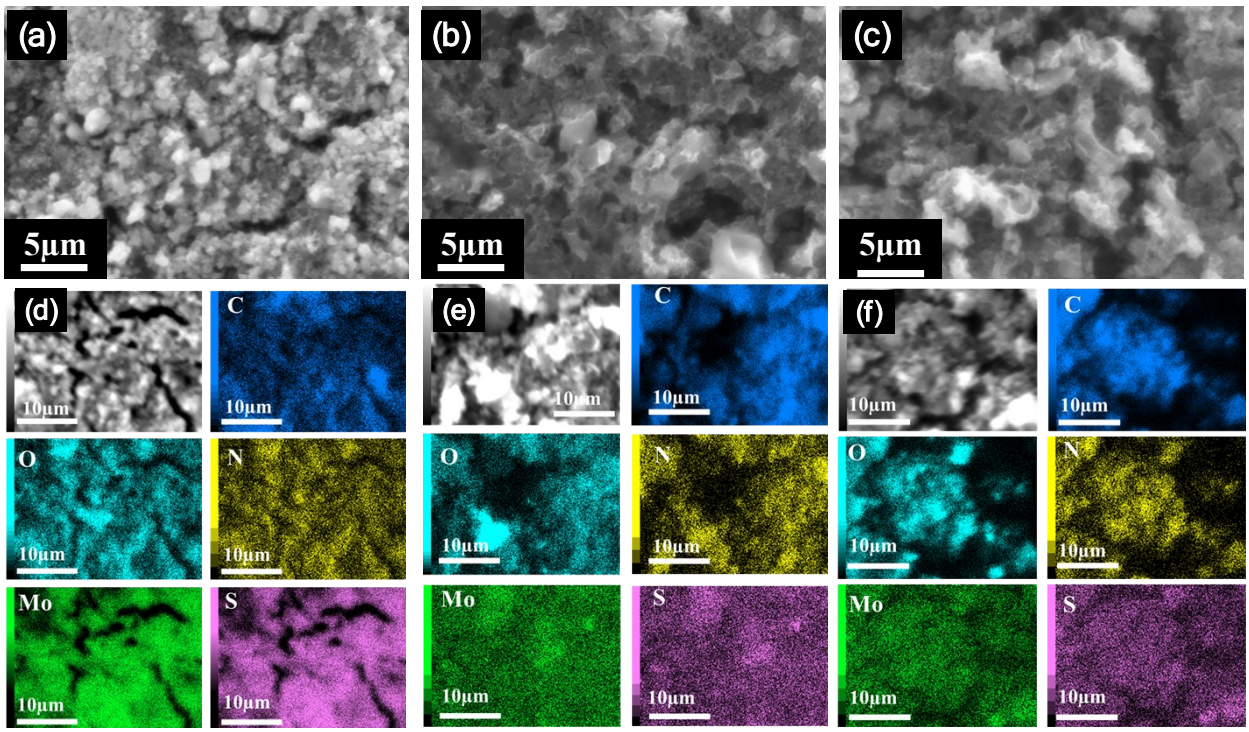

Figure S13. SEM and elemental mapping of the (a, d) pristine, (b, e) anode, and (c, f) cathode Electrodes

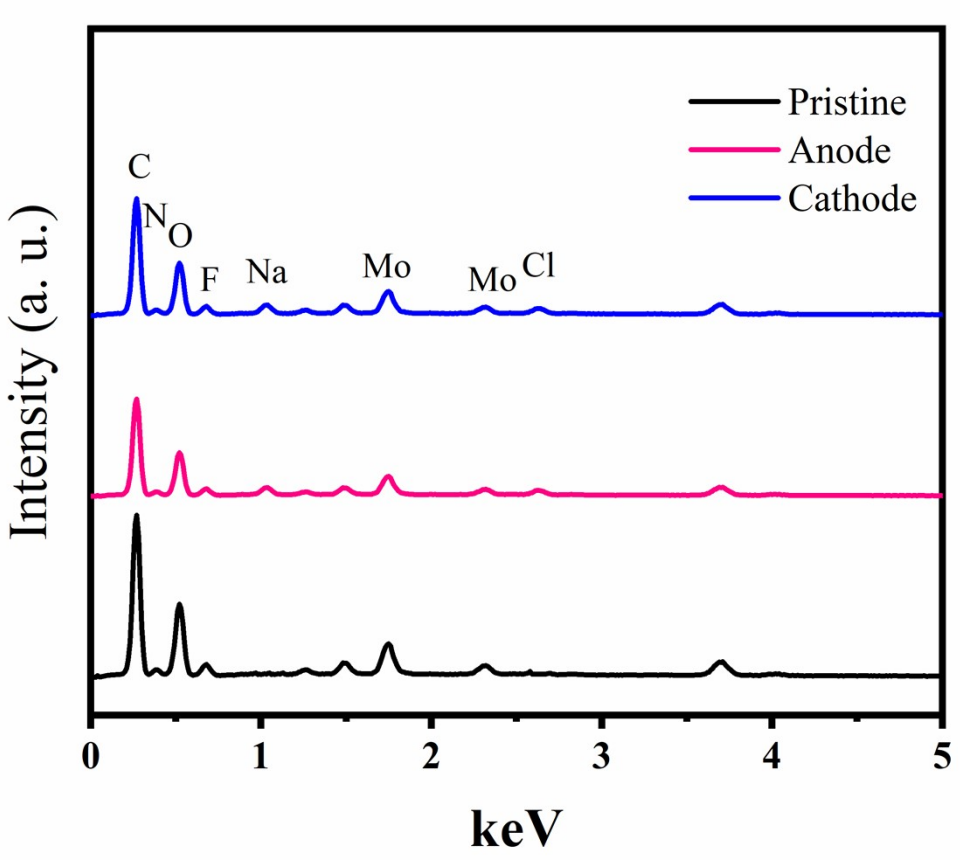

Figure S14. EDX spectra of pristine, anode cathode electrodes

Table S3 The normalized surface chemical composition of the pristine, anode, and cathode electrodes were analyzed using EDX via atomic percentages

Element	Pristine	Cathode	Anode
C	66.4	62.0	60.3
O	18.2	22.5	25.1
N	2.5	3.2	3.01
Mo	4.3	4.1	3.86
S	8.6	8.2	7.72

Table S4. Comparison of CDI`s key performance and operating conditions

Electrode / carbon type	**Mode & control**	**Voltage**	**Feed concentration of NaCl**	**SAC, SAR & stability**	**Energy consumption& charge efficiency**	**Ref.**
MoS_2/N-doped ordered mesoporous carbon (MoS_2/NOMC)	Symm. Batch mode/ CV	1.6 V	250 mg L^{-1}	SAC 30.4 mg g^{-1}, NR, 93 % after 10 cycles	NR and 70%	1
MoS_2@CNT–carbon spheres (MoS_2@CNT-CS)	Asymm. Batch mode, CV	1.2 V	500 mg L^{-1}	SAC 25.35 mg g^{-1}; SAR 3.9 mg g^{-1} min^{-1}, 98% after 30 cycles	NR and 84.7%	2
Flower-like MoS_2 on N-doped carbon spheres (MoS_2@NCS-800)	Symm. Batch mode/ CV	1.4 V	2000 mg L^{-1}	Max SAC 59.9 mg g^{-1} 100 cycles	NR and 72.4 %	3
1T-MoS_2/C hollow carbon microspheres	Symm. Batch mode/ CV	1.2 V	500 mg L^{-1}	SAC 48.1 mg g^{-1} , NR, NR	NR	4
C@MoSP carbon-embedded MoS_2–P	Asymm. Batch mode/ CV	1.2 V	500 mg L^{-1}	SAC 20.04 mg g^{-1}, NR, 100 % after 50 cycles	0.74 Wh/g and 50.5%	5
MoS_2–graphene hybrid	Symm. Batch mode/ CV	1.2 V	100 mg L^{-1}	19.4 mg g^{-1}, NR, 90 after 50 cycles	NR	6
Ce-MoS_2 (no carbon)	Symm. Batch CDI, CV	1.2 V	400 mM	SAC 8.81 mg g^{-1}, NR, NR	NR	7
AC//MoS_2@MXene	Symm. Batch CDI, CC		500 mM	SAC 35 mg/g, SAR 2.6 mg g^{-1} min^{-1}), and 96% after 40 cycles	0.26 kWh/kg	8
P-CNF/N-CNF	iCDI, Batch CDI., CC		500 mg/L	30.4 mg/g	86.2 kJ/mol and 85.70 %	9
MoS_2/NDC	Symm. Single pass/ CV	1.4 V	350 mg/L NaCl	SAC 42.9 mg g^{-1}, SAR 2.24 mg g^{-1} min^{-1}	11 kWh/kg and ~70%	This work.

				100 % after 350 cycles		

NR = Not reported

CV= Constant Voltage

CC= constant current

i-CDI= inverted CDI

References

1 S. Tian, X. Zhang and Z. Zhang, *Chemical Engineering Journal*, 2021, **409**, 128200.

2 Y. Cai, W. Zhang, R. Fang, D. Zhao, Y. Wang and J. Wang, *Desalination*, 2021, **520**, 115325.

3 T. K. A. Nguyen, T.-H. Wang and R. Doong, *Desalination*, 2022, **540**, 115979.

4 Y. Zhang, S. Fan, S. Gong, H. Liu, H. Xu, J. Qi, H. Wang, C. Li, W. Peng and J. Liu, *AIChE Journal*, 2024, **70**, e18417.

5 M. Zhao, Z. Zhao, X. Ma, J. Zhao, M. Ye and X. Wen, *Electrochim. Acta*, 2021, **387**, 138494.

6 J. Han, T. Yan, J. Shen, L. Shi, J. Zhang and D. Zhang, *Environ. Sci. Technol.*, 2019, **53**, 12668–12676.

7 F. Xing, T. Li, J. Li, H. Zhu, N. Wang and X. Cao, *Nano Energy*, 2017, **31**, 590–595.

8 Y. Cai, Y. Wang, L. Zhang, R. Fang and J. Wang, *ACS Appl. Mater. Interfaces*, 2022, **14**, 2833–2847.